Applied Surface Science 531 (2020) 147347

Contents lists available at ScienceDirect

Applied Surface Science

journal homepage: www.elsevier.com/locate/apsusc

Electronic transport properties of graphene with Stone-Wales defects and multiple vacancy chains: a theoretical study

Hao Wang[a,c], Yihan Wang[a], Bin Bai[b], Xun Guo[a,*], Jianming Xue[a,c]

[a] State Key Laboratory of Nuclear Physics and Technology, School of Physics, Peking University, Beijing 100871, PR China
[b] National Key Laboratory for Surface Physics and Chemistry, China Academy of Engineering Physics, Jiangyou 621908, PR China
[c] CAPT, HEDPS, and IFSA Collaborative Innovation Center of MoE, College of Engineering, Peking University, Beijing 100871, PR China

ARTICLE INFO

Keywords:
Stone-Wales defect
Density functional theory
Non-equilibrium Green's function method
Graphene field effect transistor

ABSTRACT

Recent advances in controlled synthesis of graphene nanodevices urge the understanding of various defects' effect on the electronic transport properties, such as Stone-Wales defects, single vacancy, double vacancies and multiple vacancy chains. In this work, we systematically investigated these defects in single-layer graphene, by using first principle calculations combined with the non-equilibrium Green's function method. The calculated current-voltage curves reveal that these defects can lead to current decrease compared with pristine graphene. Besides, corresponding transmission spectra and device density of states indicate that some defect induced electron states can strongly enhance the transport of electron between electrodes at certain energy levels, while others are only localized around the defect sites. Moreover, the distinct results of graphene with multiple vacancy chains demonstrate that both the number and arrangement of vacancy defects could affect the electronic transport properties of graphene nanodevices. We also verified that these vacancy defects could be easily identified by using a small source-drain voltage and sweeping the gate voltage applied on the graphene field effect transistors. These results are helpful to further understand vacancy defects' impact on the transport properties of graphene nanodevices, and inspiring to tune the electronic behaviors of two-dimensional nanodevices through controlled defect engineering modifications.

1. Introduction

Since its successful fabrication by mechanical exfoliation in 2004 [1], graphene has attracted extensive interest worldwide, for its unique physical structures and fantastic electronic transport properties, such as anomalous quantum Hall and confinement effect [2,3]. Because of its conical energy band structure with linear dispersion near K-point, electrons in the graphene behave as mass-less Dirac fermions, which contributes to a very high carrier mobility (2.5×10^5 cm^2 V^{-1} s^{-1}). However, limited by the synthesis techniques, there are always some inevitable defects exist in every graphene monolayer. Besides that, tuning the electrical properties of graphene through controlled structure modifications is also of great interest [4–11]. Therefore, it is of great importance to extensively understand the electronic properties of these defects, for the potential applications, such as graphene-based nanodevices [12].

Many previous ion/ electron beam irradiation experiments and theoretical calculations have already demonstrated that vacancy defects could affect the charge carrier mobility of graphene in the mesoscale regime due to different carrier scattering mechanisms [13–22]. For example, Zion et al. observed that the increase of vacancy defect concentration in graphene could lead to a transformation of conductivity from metallic to weak localization, and even strong localization through measurements of the temperature dependence of conductivity [23]. Nakaharai et al. found that the carrier transport of graphene with localized low-density vacancy defects is dominated by strong localization of carrier at the defect localization sites [21]. More recently, Naitou et al. observed the metal-insulator transition of graphene at about 1.2 % vacancy density due to Anderson localization effect [22]. However, these simple typical defects cannot fully represent the properties of real graphene samples, and the influence of complex large defects is still a difficult problem urgently needs to be explored.

In order to theoretically investigate the impacts of a specific defect in graphene nanodevices, only the ballistic transport model can be used to describe the transport properties of electrons, since the traditional drift-diffusion model is no longer applicable [20]. As we know, with the approaching of physical limit of bulk silicon complementary metal-oxide-semiconductor (CMOS), low dimensional materials with

* Corresponding author.
E-mail address: guo.xun@pku.edu.cn (X. Guo).

https://doi.org/10.1016/j.apsusc.2020.147347
Received 15 March 2020; Received in revised form 17 July 2020; Accepted 22 July 2020
Available online 30 July 2020
0169-4332/

ultrashort channels have been proposed as potential candidates of the next-generation transistors, such as graphene, transition metal sulfides (TMS), and phosphorene [24–27]. For example, Jiang et al. observed specific vacancy defects could open a band gap in graphene, and thus strongly promote the switch ratio (I_{on}/I_{off}) of graphene field effect transistors (FET) [28]. Mendez et al. demonstrated that grain boundary (GB) generally preserve the semiconductor properties of graphene, but some specific asymmetric GBs could open a moderate transport gap [29]. By using ballistic transport model, Zaminpayma et al. have successfully found that the single vacancy and Stone-Wales defects could decrease the current through the graphene nanodevices, accompanied by defect induced electron transmission peaks [30], which means this method can hopefully be used to study the influence of multiple vacancy chains on the electronic transport properties of graphene nanodevices.

In this article, we explored this problem by applying systematical investigation on the electronic transport properties of graphene nanodevices with different typical vacancy defects [31–35] using the density functional theory (DFT) with the non-equilibrium green function (NEGF) method [36,37]. Our first principle calculations indicate that these vacancy defects suppress the current compared with the pristine graphene, depending on the number and arrangement of vacancies. More importantly, the bias voltage-dependent transmission spectra and corresponding projected local density of states demonstrate that some defect induced electron states can strongly enhance the transport of electrons between electrodes at certain energy levels, while others are just localized around the defect sites.[20] Besides that, a novel phenomenon is observed that the increase of vacancies along the transport direction will not degrade the performance of graphene nanodevices. Further calculations reveal that the formation energy of multiple vacancy chains depends on the number of vacancy contained instead of the vacancy arrangement. Finally, we have verified a previous scheme [38] that these defects could be directly identified according to their specific transport peaks by using a small source-drain voltage and sweeping the gate voltage applied on the graphene FETs, which enable the non-destructive inspection of nanodevices and may by applied in future nano-electronic industry. Overall, our work is helpful to understand vacancy defects' impact on the transport properties of graphene nanodevices, and inspiring to tune the electronic behaviors of two-dimensional nanodevices through controlled defect engineering modifications.

2. Methods

Following previous researches [28,30], a two-probe transport system comprised of three parts: the left/ right electrode, and the central scattering region, was applied in the following investigation, as illustrated in Fig. 1. The center region of pristine graphene sample contains 288 carbon atoms, with dimensions of 17.16 × 44.60 Å^2. Unlike graphene nanoribbon and nanotube, periodic boundary condition was applied along B axis to avoid any edge effects. Besides, a 10 Å vacuum along the axis A was employed to avoid the interactions between the periodic graphene mirrors. The steady state quantum transport calculations were performed by using first principle density functional theory (DFT), with the general gradient approximation (GGA) combined with the non-equilibrium Green's function (NEGF) method [36,37], as implemented in the Atomistix ToolKit (ATK, version 2018.06-SP1-1) program package [39–41]. The Perdew-Burke-Ernzerhof (PBE) exchange-correlation functional was used with a real-space mesh cutoff of 75 Hartree [42], and the Norm-conserving Fritz-Haber-Institute (FHI) pseudopotential was used to describe the core electrons [43].

The wave function was expanded by the double-zeta plus polarization (DZP) basis set for all atoms. This FHI (DZP) setting is widely used in previous articles to study the influence of defects on the transport properties of graphene and its derivations including nanotubes and nanoribbons [19,20,44–49]. Besides that, the FHI (DZP) setting could give nearly the same band structure and current-voltage ($I-V$) curves compared with the newly-developed PseuDojo (Ultra) [50] and SG15 (Ultra) [51,52] settings, as discussed in supplementary materials. The structural relaxations of each two-probe system with typical defects were performed by using the LBFGS optimizer method [53] and allowed until the absolute value of force acting on each carbon atom was less than 0.01 eV/Å, with the Brillouin zone of the electrode was sampled with 1×3×300 Monkhorst-Pack k-points along the A, B, C directions, respectively [54]. The current (I) through the transport system at a given bias voltage V_b and gate voltage V_g was calculated from the Landauer-Büttiker formula [55,56]:

$$I(V_b, V_g) = \frac{2e}{h}\int_{-\infty}^{\infty} T(E, V_b, V_g)[f_L(E-\mu_L) - f_R(E-\mu_R)]\mathrm{d}E,$$

where $T(E, V_b, V_g)$ is the transmission coefficient, f_L and f_R are the Fermi-Dirac distribution functions for the source and drain, while μ_L and μ_R are the electrochemical potentials of the left and right electrodes, respectively. The gate controlling effect was calculated by solving the Poisson's and Kohn-Sham's equations self-consistently. The gate and dielectric regions were treated as the boundary conditions of the Poisson's equation [36]. The energy self-convergence criterion was set to 10^{-5} eV. In order to get reliable current results, much more sampling k-points (K_B = 20) were used for the transmission spectrum calculation. The density mesh cutoff (E_{grid}), the sampling k-points K_B, K_C and the specific K_B for transmission spectrum calculations are examined to make the current deviation of pristine graphene nanodevices at V_b = 2 V (V_g = 0 V) less than 0.2% (see the supplementary material for more detail).

It is noteworthy that graphene with odd number of vacancies is reactive and unstable [57], so in this work we only considered the multiple vacancy chains that contain even vacancies. Although the spin-polarized states may appear in graphene with or without defects, they usually would become unstable at finite temperature due to the weakness of magnetism, compared with spin-unpolarized state [58,59]. Besides, previous calculations indicated that graphene with even number vacancies usually doesn't have magnetic moment [60]. Thus, only spin-unpolarized calculations were performed in this work. Considering the weak electron-phonon coupling in graphene [61–64] and expensive computational cost, the phonon-assisted electronic transport has been neglected in the current calculations [20,65,66].

3. Results and discussion

3.1. Stone-Wales defect and single vacancy

Transport properties of graphene with Stone-Wales (SW) defect and the single vacancy (SV) were firstly investigated in this work, as they were widely considered to be the simplest and most important defect types [67,30]. Fig. 1 shows the structures of Stone-Wales defects (SW_1, SW_2) and single vacancy (SV) after the geometry optimization, which have already been observed experimentally using the high-resolution transmission electron microscopy [31,33,34,68]. As shown in Fig. 1 (a) and (b), the optimized Stones-Wales defect are illustrated by colored polygons. The bond length of pristine graphene is 1.43 Å , and about 1.33 Å for SW defect, which are in good agreement with previous results [30].

Fig. 2(a) shows the self-consistently computed current-voltage ($I-V_b$) curves of pristine graphene and graphene with SW_1, SW_2 and SV_1 defect at the bias voltage range of 0 ~ 2 V. As illustrated in Fig. 2(a), the behavior of these $I-V_b$ curves is non-linear. Moreover, the SW_1 and SW_2 defects have little suppression effect on the electronic transport as compared with the prefect one, while the SV_1 defect obviously suppresses the current at high bias voltages. These phenomena are in good accordance with previous density functional-based tight binding (DFTB) transport calculations [30,28].

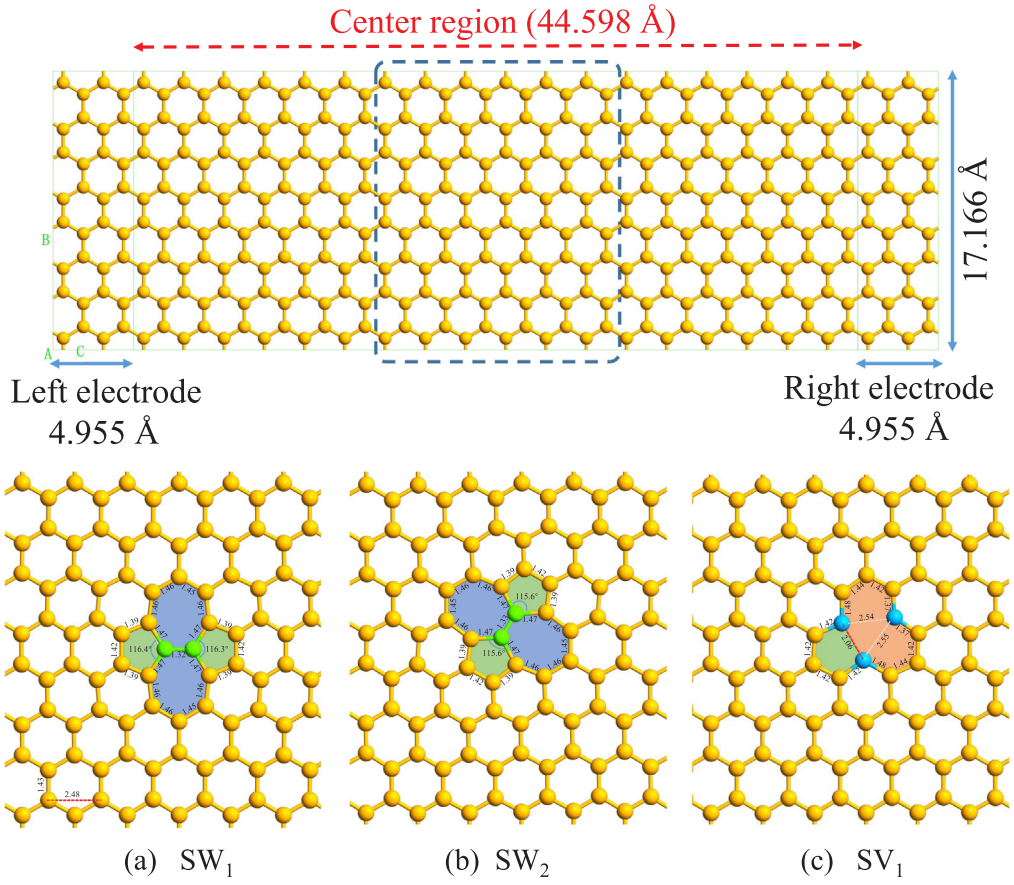

Fig. 1. Top: Schematic diagram of the two-probe pristine graphene transport system. The length of center region and left/right electrode is about 44.598 Å and 4.955 Å, respectively. The configurations of graphene with Stone-Wales defects (a) SW_1, (b) SW_2, and single vacancy (c) SV_1 after geometry optimization. The green atoms are rotated 90° in advance to form the Stone-Wales defect, while the blue atoms are nearest neighbor atoms around the single vacancy.

To explain the different behavior of $I-V_b$ curves, we further compute the bias-dependent transmission spectra, which could represent the coupling between electrodes and central defective regions [48]. As shown in Fig. 3, the bias depended voltage-dependent transmission spectra within the bias voltage range 0 ~ 2 V of pristine graphene and graphene with SW_1, SW_2 are nearly the same, while a transmission peak near the Fermi level is observed above 0.8 V for graphene with SV_1. In detail, when the bias voltage V_b is below 0.8 V, the electron transmission probability near the Fermi level increases gradually, which contributes to the current increase most for all the four cases. However, when the bias voltage V_b is above 0.8 V, the electron transmission probability keeps almost unchanged around the Fermi level, while the transmission probability of electrons near −0.5 and 0.55 eV begins to increase gradually, for pristine graphene, and graphene with SW_1, SW_2 defects. In other words, high bias voltage results in improved transmission of electrons at energy near −0.5 and 0.55 eV, which dominates the increase of current.

However, for the case of SV_1, a new electron transmission peak occurs near the Fermi level and the earlier mentioned two transmission peaks near −0.5 and 0.55 eV disappear above 0.8 V, as compared to pristine graphene, which means the SV_1 defect could strongly enhance the transport of electron near Fermi level, and suppress the transmission of electrons at other energy levels when the V_b is above 0.8 eV. The transmission peak near the fermi level of graphene with SV_1 defect, and sharp transmission decrease near 0.6 eV of graphene with SW_1 defect, have already been observed in previous first-principle calculations

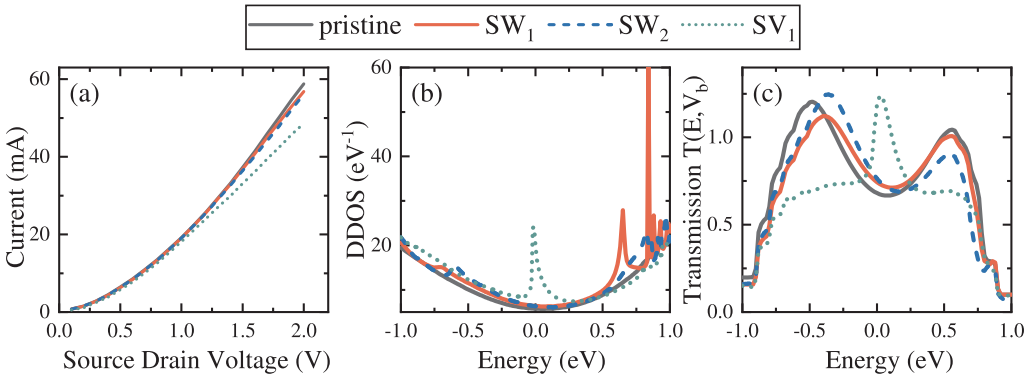

Fig. 2. (a) The $I-V_b$ curves of pristine graphene and graphene with SW_1, SW_2 and SV_1 defects at the bias voltage range of 0 ~ 2 V. (b) The corresponding device density of states at V_b = 2.0 V. (c) The corresponding transmission spectra at V_b = 2.0 V.

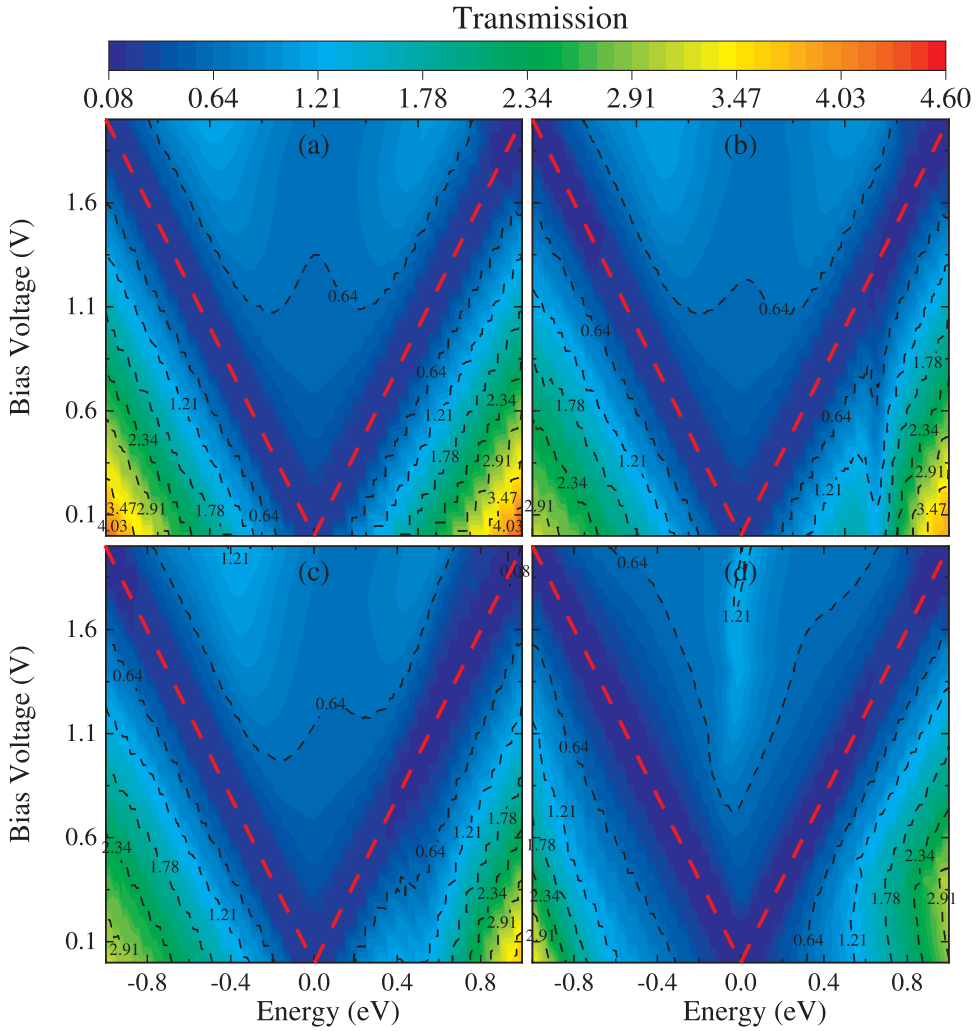

Fig. 3. The bias voltage-dependent transmission spectra of (a) pristine graphene, and graphene with (b) SW_1, (c) SW_2, (d) SV_1, respectively. The red dashed lines indicate the top and bottom limitation of the bias voltage V_b window. (For interpretation of the references to colour in this figure legend, the reader is referred to the web version of this article.)

[30,38], which could also be treated as a verification of our results.

To find out the reason of different electron transmission of the SW and SV defects, we further calculate the corresponding device density of states (DDOS) and electron transmission spectra of pristine graphene, graphene with SW_1, SW_2 and SV_1 defects at the bias voltage V_b = 2.0 V. Note that in Fig. 2(c), we only plot the transmission spectra of the pristine graphene and graphene with SW_1, SW_2, SV_1 defects at the bias voltage V_b = 2.0 V, whose integration area could represent the currents through these devices at 2.0 V. Therefore, the transmission change of electrons shown in Fig. 2(c) could only contribute to the currents at 2.0 V, which will not be reflected in the $I - V_b$ plots. Furthermore, as shown in Fig. 2(b-c), for the case of SV_1, a clear state peak occur near the Fermi level, in accordance with the enhanced transmission peak shown in Figs. 2(c) and 3(d). In other words, the defect induced electron states near the fermi level by the SV_1 defect when V_b is above 0.8 V can strongly enhance the transport of electron between electrodes at the fermi level and therefore we call these states "the defect induced resonant transport states". Meanwhile, as for SW_1 and SW_2 defects, there are also several defect induced electron state peaks near 0.6 and 0.8 eV as shown in Fig. 2(b). However, no obvious improved electron transmission is observed from the corresponding transmission spectra shown in Fig. 2(c), which suggests that these defect states are just localized around the defects and do not improve the corresponding electron transport. Therefore, we call these electron states "the defect induced localized states". Previous studies have already revealed that some defect induced electron states in defective graphene may localize around the defect sites which therefore not participate to the transport of charge carriers but will rather degrade it [20]. Similar phenomena in graphene nanodevices with multiple vacancy chains have also been analyzed and discussed in the following section.

3.2. Multiple vacancy chain

The multiple vacancy (MV) chains are also easy to be introduced deliberately by using the nano-patterning technology [69,34]. However, it is nearly impossible to consider all potential atomic arrangements of vacancy defects. To simplify this problem, we focused on three characteristic structures of MV chains as an example: MV along the zigzag channel (MV_l), across the zigzag channel (MV_h), and obliquely across the zigzag chain (MV_s). Fig. 4 and S1 show the configurations of graphene with vacancies chains before and after the geometry optimization to make a brief illustration, and detailed structure of 4 V are also provided in Fig. S1 as a representative.

First we concentrate on MV chains that have same type but different number of vacancies. As shown in Fig. 5(a), for type MV_l, it seems that the current difference of graphene with $2V_l$, $4V_l$, $6V_l$, $8V_l$ and $10V_l$ (when V_b between 0 ~ 2.0 V) is less than 1 μA, which demonstrates that the increase of vacancies along the zigzag chain would not suppress the

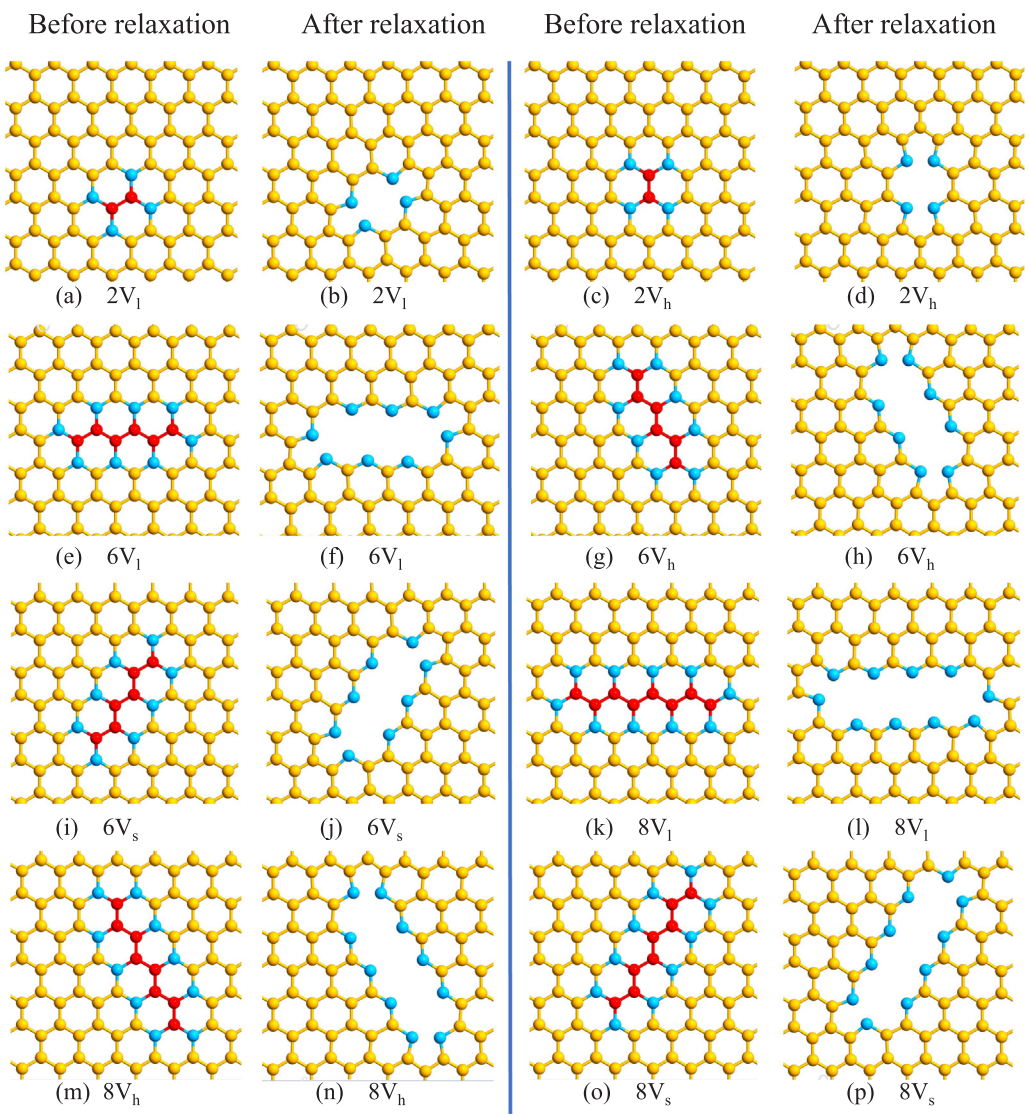

Fig. 4. The structures of some multiple vacancy chains before and after geometry optimization. The red atoms represent the carbon atoms deleted to form specific defects, while the blue atoms nearest the vacancies are mapped to demonstrate the structural modifications during the geometry optimization. (For interpretation of the references to colour in this figure legend, the reader is referred to the web version of this article.)

transport current further. Besides, it's surprising to find $I(4V_l) > I(2V_l)$, which is against the general instinct that more electron losses cause more current suppression, and also proves that the influence of vacancy arrangement is as significant as the number of vacancies [30].

For this reason, we calculate the electron transmission spectra at 2.0 V for graphene with $2V_l$, $4V_l$, $6V_l$, $8V_l$ and $10V_l$. As shown in Fig. 5(d), the transmission spectra of these five cases are almost the same when the electron energy is above 0.3 eV, with a stable peak near 0.36 eV, which can be treated as a typical signature of the MV_l defect. Another transmission peak near -0.3 eV also becomes sharper and moves to -0.4 eV, accompanied with the slight transmission decrease between -0.9 ~ -0.2 eV. The synergistic effect of these two trends leads to the little difference between the calculated current of graphene samples with $2V_l$, $4V_l$, $6V_l$, $8V_l$ and $10V_l$ defects.

However, although the calculated $I - V_b$ curves are nearly unchanged, the transmission spectrum shown in Fig. 5(d) indicated that the defect induced resonant transport energy has been changed due to the different number of vacancy. Therefore, in Fig. 6, we calculate the projected local density of states (PLDOS) of graphene with $2V_l$, $4V_l$ and $6V_l$ at $V_b = 2.0$ V, which can illustrate the space-resolved electron densities of states. A clear defect induced resonant transport state can be observed at 0.36 eV for all the three cases, which is corresponding to the sharp transmission peak near 0.36 eV as shown in Fig. 5(d). Besides, two defect induced localized states of $6V_l$ can also be found in Fig. 6(c), while no corresponding improved electron transmission occurs in Fig. 5(d). The similar phenomena in the cases of grephene with SW_1, SW_2 and SV_1 defects occur again in graphene with MV chains that some defect induced electron states could strongly enhance the electron transport at their energy levels, while others are only localized around the defect sites and barely improve the corresponding electron transmission [20].

However, things are more complicated for graphene with MV_h and MV_s defects. It can be seen from Fig. 5(b, c) that $I(2V_h) \approx I(4V_h) \approx I(6V_h) > I(8V_h) > I(10V_h)$, while $I(2V_s) > I(4V_s) > I(6V_s) \approx I(8V_s) \approx I(10V_s)$. It seems for MV_h defects, at the beginning the increased vacancy defects have little suppression effect on the transport currents, while when the number of vacancy is above 6, the currents decrease with the increase of vacancy defects. However, for MV_s defects, the currents decrease with the increase of vacancy defects at first, while when the number of vacancy is above 6, the increased vacancies don't degrade the current anymore. These phenomena can be explained by the corresponding transmission spectra. As shown in Fig. 5(e), for MV_h defects,

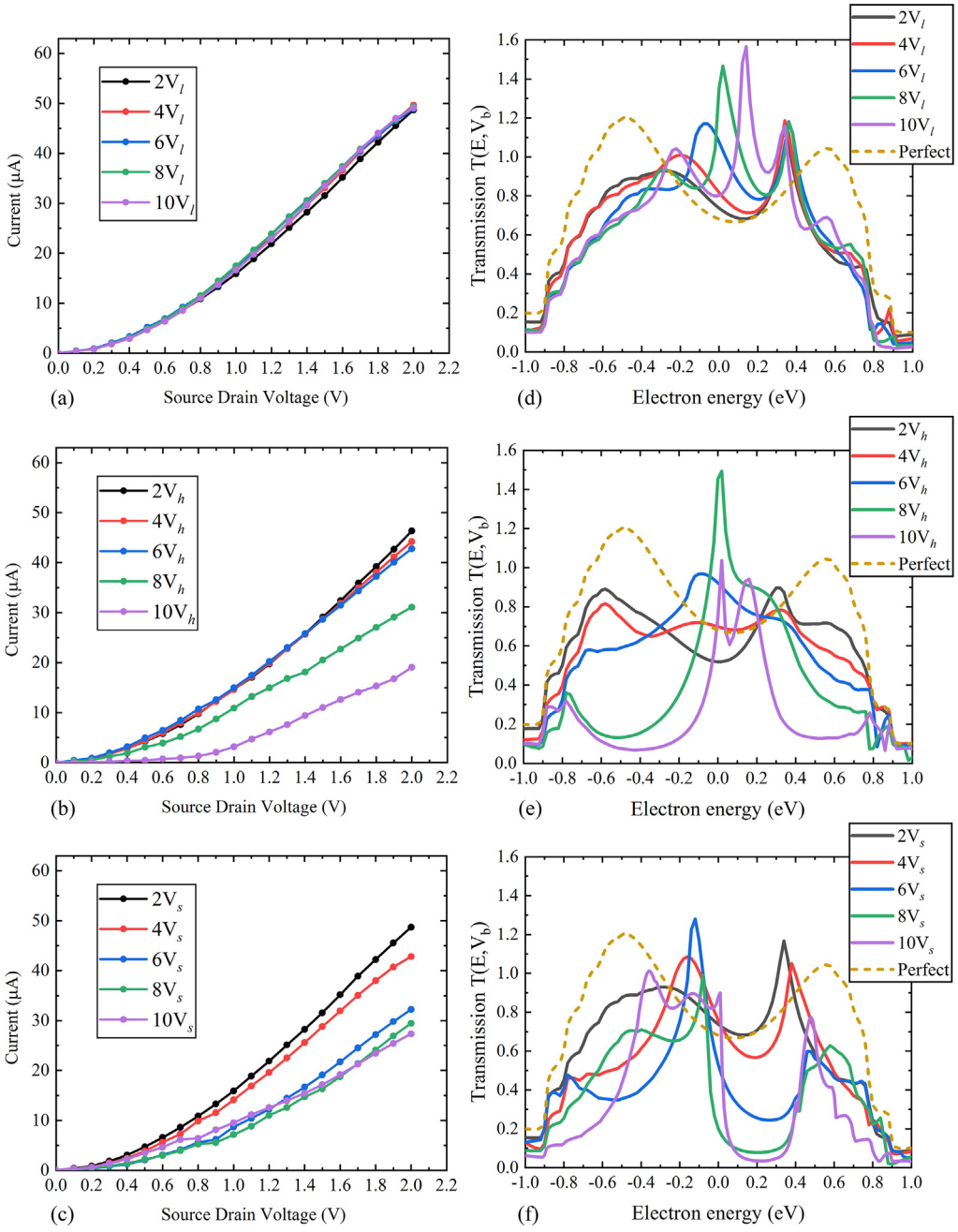

Fig. 5. The $I - V_b$ curves of graphene nanodevices with (a) MV_l, (b) MV_h and (c) MV_s defects when M = 2, 4, 6, 8 and 10. (d–f) The corresponding transmission spectra at $V_b =$ 2.0 V.

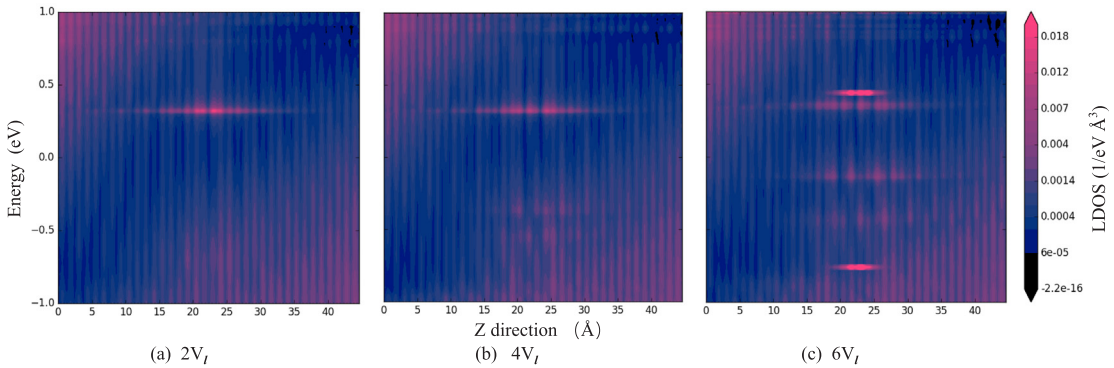

Fig. 6. The projected local Density of states of graphene nanodevices with (a) $2V_l$, (b) $4V_l$ and (c) $6V_l$ defects, respectively.

the transmission peaks near −0.6 and 0.5 eV decrease and disappear with the increase of vacancy defects, while a new transmission peak near the Fermi level occurs and enlarges. At first, the current decrease caused by the transmission decrease can be remedied by the new induced transmission peak near the Fermi level, which results in little difference between $I(2V_h)$, $I(4V_h)$ and $I(6V_h)$. Then the effect of transmission decrease cannot be complemented by the new induced transmission peak, the current decrease $I(6V_h) > I(8V_h) > I(10V_h)$ is clearly observed in Fig. 5(b). As for MV_s defects in Fig. 5(f), the transmission probability of electrons between 0.0 ~ 0.4 eV decreases sharply at first, which causes the current decrease $I(2V_s) > I(4V_s) > I(6V_s)$. However, when the transmission probability is near 0 for electrons between this energy range, the contribution of these electrons can be neglected and the electrons between −0.8 ~ −0.2 eV dominate the transport current, which results in $I(6V_s) \approx I(8V_s) \approx I(10V_s)$. In other words, the diverse electron transmission spectra could account for the different $I - V_b$ curves' behaviors of graphene with typical defects.

We have also compared the $I - V_b$ curves of graphene nanodevices with MV_l, MV_h, MV_s defects made of equal vacancies to find out whether the arrangements of vacancy defects could affect the transport properties of graphene. As shown in Fig. 7, the current suppression effect is always least for MV_l defects, while there is no clear relationship between MV_h and MV_s defects. As can be seen from Fig. 5, the current suppression effect of MV_h defects increases with the number of vacancy, while is opposite for MV_s defects. Therefore, it is not surprised to see that $I(6V_l) > I(6V_h) > I(6V_s)$ while $I(10V_l) > I(10V_s) > I(V_h)$.

To display the impact of defect configuration on the electron transmission at the same energy, we have plot the corresponding transmission spectra of graphene with $6V_l$, $6V_h$ and $6V_s$ at the bias voltage (V_b = 2.0 V). As shown in Fig. 8(a), the transmission of electrons at the same energy varies with the defects contained in graphene, for example $T(6V_l) > T(6V_h) > T(6V_s)$ for electrons at 0.36 eV. We further exhibit the eigenstates at Γ point of $6V_l$, $6V_h$ and $6V_s$ at the eigenvalue of E = 0.36 eV when the bias voltage V_b = 2.0 V. As shown in Fig. 8(b-d), much more electron states are scattered back by the $6V_s$ defect than $6V_l$ and $6V_h$ defects, thus only a few electrons could access the right electrode, which is also corresponding to the relative transmission coefficients $T(6V_l) > T(6V_h) > T(6V_s)$ at 0.36 eV shown by the green dash line in Fig. 8(a). The discrepant transmission behaviors of electrons at the same energy indicates the characteristic features of various defects. Above all, we have demonstrated that both the number and arrangement of vacancy defects could affect the transport properties of graphene nanodevices.

3.3. Defect formation energy

In order to investigate the stability of graphene with these defects, we have calculated the defect formation energy E_f of various defects concerned in this work: $E_f = E_{defect} - E_{total} + N\mu_C$, where E_{defect} is the total energy of the defective graphene, E_{total} is the total energy of the pristine graphene, N is the number of removed atoms, and μ_C is the C chemical potential (the mean C atomic energy in pristine graphene in this work).

Previous articles have reported that the formation energy E_f of SV, SW and 2 V defects is about 7.9 [70], 5.0 [71,72] and 8.0 eV [71,72], respectively, which is in good accordance with our calculations and indicates the FHI pseudopotential with the DZP basis set could give a reliable description of the graphene systems concerned in this work [38]. As for vacancy defects that contain more than four vacancies, previous articles have indicated that the formation energy of the dislocation vacancy defects (similar to our work) including 4 V, 6 V, 8 V, 10 V is about 14, 21, 26 and 30 eV [73], respectively, which is also in good agreement with our results. Besides that, as shown in Table 1, it's worthy noted that the E_f of multiple vacancy chains depends on the number of vacancy contained instead of the vacancy arrangement, for example E_f $(2V_l) < E_f$ $(4V_l) < E_f(6V_l) < E_f(8V_l) < E_f(10V_l)$ while

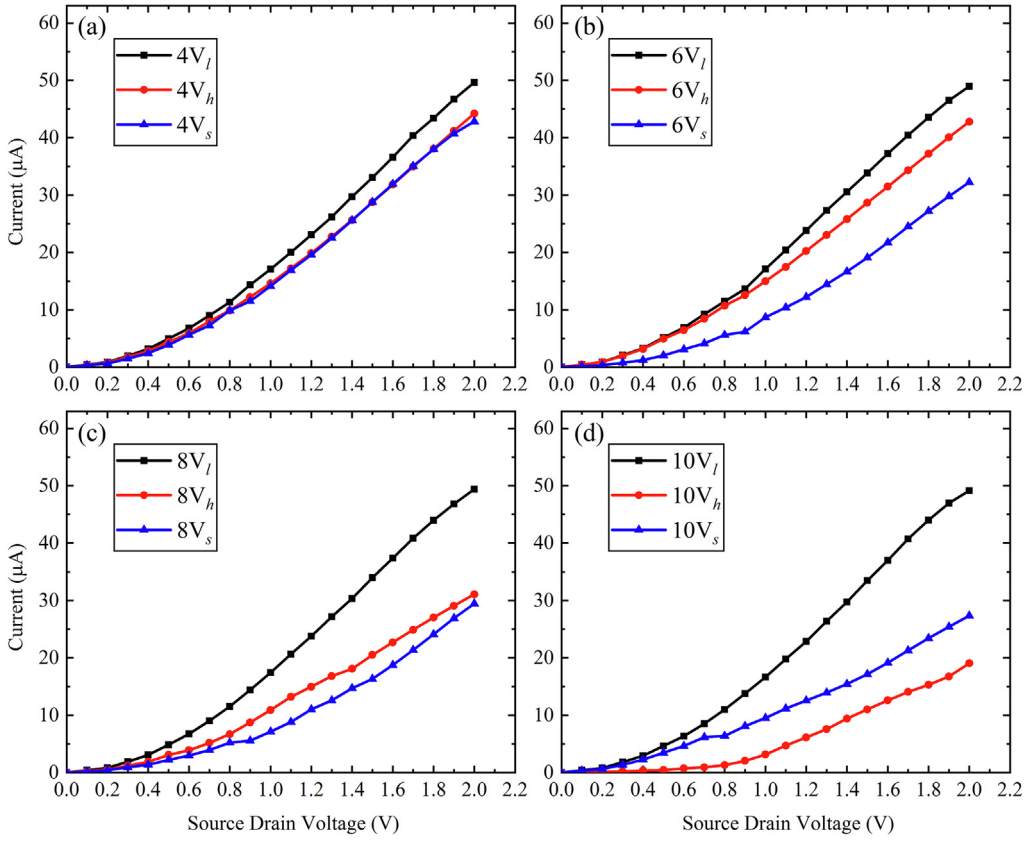

Fig. 7. The $I - V_b$ curves of graphene with MV_l, MV_h and MV_s defects when M = (a) 4, (b) 6, (c) 8 and (d) 10, respectively.

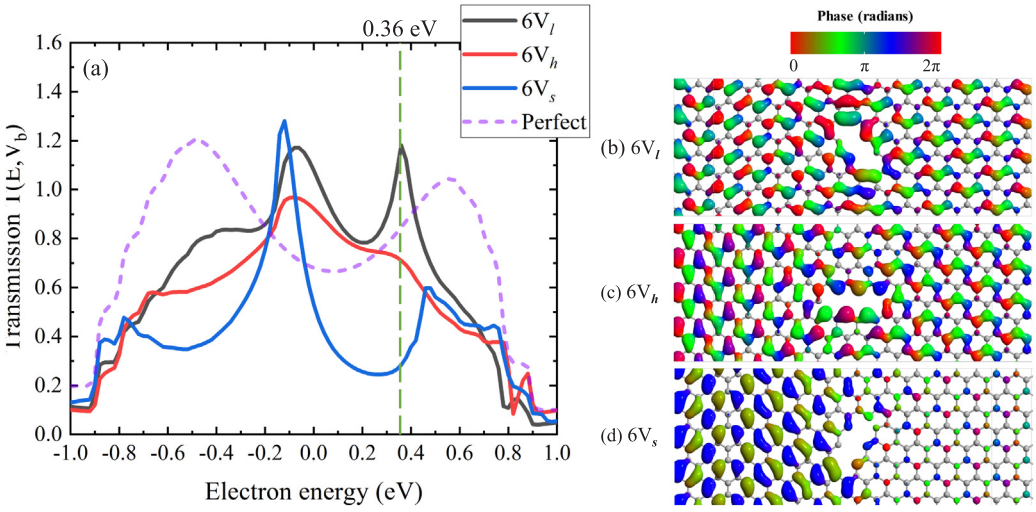

Fig. 8. (a) The transmission spectra of pristine graphene and graphene with $6V_l$, $6V_h$ and $6V_s$ defect at $V_b = 2.0$ V, respectively. The green dashed indicates $T(6V_l) > T(6V_h) > T(6V_s)$ for electrons at 0.36 eV. The eigenstates (at the Γ point) of graphene nanodevices with (c) $6V_l$, (d) $6V_h$ and (e) $6V_s$ defects at an eigenvalue of $E = 0.36$ eV when $V_b = 2.0$ V, respectively. The phase and amplitude are illustrated by color and radius. (For interpretation of the references to colour in this figure legend, the reader is referred to the web version of this article.)

Table 1
The calculated defect formation energy (E_f) in graphene.

Defect	E_f (eV)	Defect	E_f (eV)	Defect	E_f (eV)
SW_1	5.26	SW_2	5.01	SV_1	8.17
$2V_l$	7.68	$2V_h$	7.92	$2V_s$	7.68
$4V_l$	14.31	$4V_h$	14.50	$4V_s$	14.29
$6V_l$	21.08	$6V_h$	21.11	$6V_s$	21.06
$8V_l$	27.83	$8V_h$	27.53	$8V_s$	27.76
$10V_l$	34.67	$10V_h$	33.78	$10V_s$	34.45

$E_f(6V_l) \approx E_f(6V_h) \approx E_f(6V_s)$, which has also been observed in previous work [73]. Although these vacancy defects have rather large formation energy values, they could be easily produced using the modern electron/ion beam lithography.

3.4. Graphene field effect transistor

Since different defects present specific transmission spectra, it is reasonable to expect whether we can identify these defects from each other simply using the $I - V$ curves. Haldar et al. proposed a method that these characteristic defect states could be obtained, by applying small bias voltage and a relatively small gate voltage, then differentiate between these defects by comparing the relative behaviors of $I - V_g$ curves [38]. According to this method, we have designed a graphene field effect transistor (FET) sample with $6V_l$, $6V_h$ and $6V_s$ defects, and calculated the corresponding $I - V_g$ curves. The schematic diagram of the graphene FETs with defects are illustrated in Fig. 9(a, b). A SiO_2 semiconductor layer with 2 Å thickness is above the graphene layer, at the distance of 1 Å. A metal gate is 3 Å right above the graphene layer and its thickness is 1 Å. The gate voltage is modeled by adding an electrostatic potential into the one-electron Kohn-Sham equation (see supplementary for more detail). In order to exhibit the characteristic behaviors of these $I - V_g$ curves, we have plot the current relative ratio using the currents at $V_g = 0$ V as a reference. The $I - V_g$ curves shown in Fig. 9(c, d) exhibit different peaks and magnitudes for graphene FETs with $6V_l$, $6V_h$ and $6V_s$ defects, which demonstrates that we could differ these defects contained in graphene FET nanodevices by recognizing the characteristic peaks of the $I - V_g$ curves directly, instead of expensive and complicated TEM characterizations. Besides, this phenomenon may also be applied to design specific nanodevices in future nano-electronics, for example the amino acid sensors and protein sequencers [74].

It's also worthy to note that the ultrashort channel graphene nanodevices shows better irradiation resistance compared with the micrometer-scale graphene devices. In previous studies, 1.2% defect density could lead to the metal-insulation transition in graphene devices [22,20]. However, graphene sample with the $10V_s$ defect, which corresponding to over 3% defect density, only results in about 50% current loss. Therefore, ultra-short channel nanodevices may have natural irradiation resistance due to the ultra-short source-drain length. Under the same irradiation environment, the electron transport will be less affected with fewer scattering defects in the much shorter channel. However, due to the challenging fabrication of two dimensional nanodevices, irradiation experiment result on such ultra-short nanodevices has not been reported yet, and further investigation on this field still remains to be explored.

4. Conclusions

In summary, we have investigated the electronic transport properties of graphene nanodevices with typical defects, including Stone-Wales defects, single vacancy, double vacancies and multiple vacancy chains. The calculated results indicate that these defects suppress the current compared to the pristine graphene, accompanied with characteristic defect induced resonant transport states and defect induced localized states. The distinct result of multiple vacancy chains demonstrates that both the number and arrangement of vacancies could affect the electronic transport properties of graphene nanodevices. Furthermore, we also verify that different defects could be easily identified according to the characteristic behaviors of $I - V_g$ curves, by using a small bias voltage and sweeping the gate voltage applied on the graphene FETs. This work would provide an inspiring perspective to modify the electronic transport behaviors of two-dimensional nanodevices through controlled defect engineering.

Author contributions

Xun Guo and Jianming Xue conceived the research. Hao Wang and Xun Guo performed the simulations and data analysis. Hao Wang, Yihan Wang and Xun Guo prepared the manuscript. All authors discussed the results, commented on the manuscript, and contributed to the writing of this article.

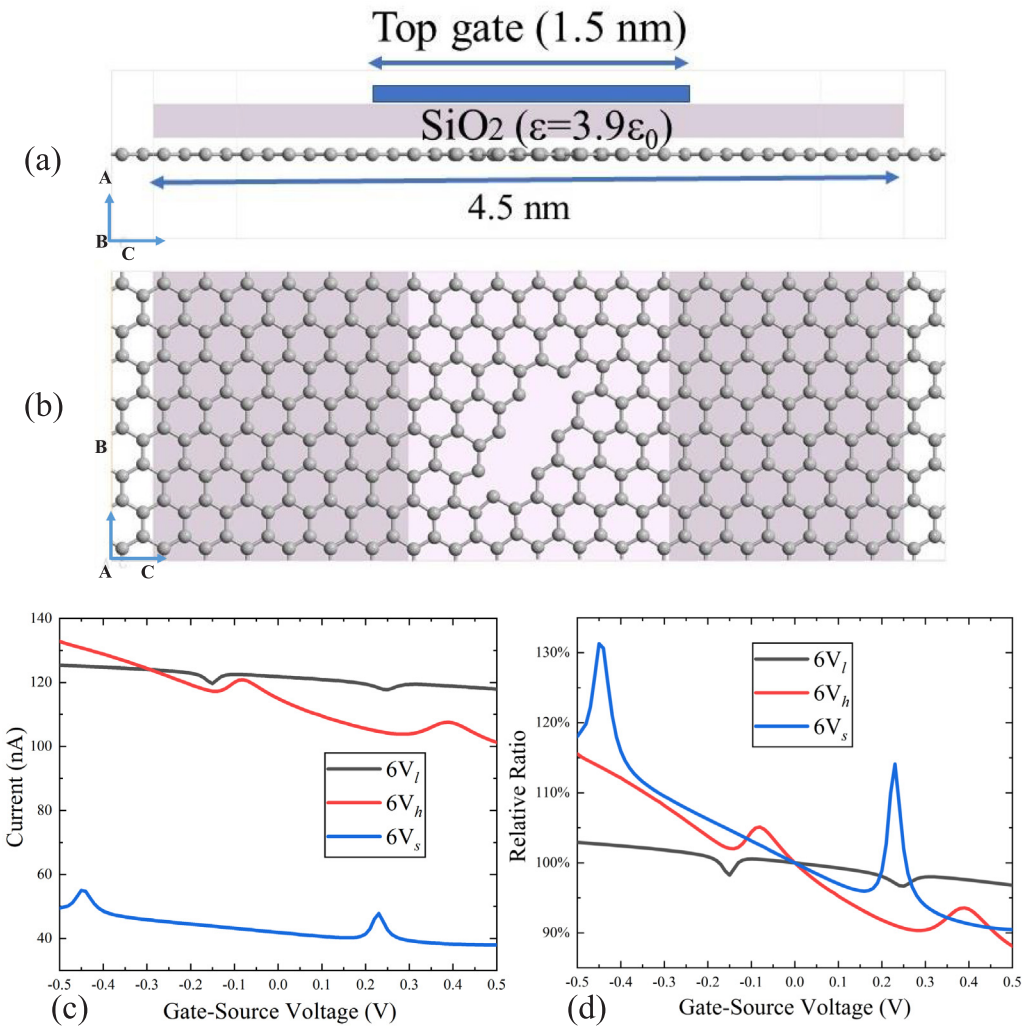

Fig. 9. The front (a) and top (b) view of the graphene FET schematic diagram. (c) The $I - V_g$ curves of graphene FET with $6V_l$, $6V_h$, $6V_s$ at $V_b = 0.1$ V. (d) The current relative ratio of graphene FET with the defect $6V_l$, $6V_h$, $6V_s$ at $V_b = 0.1$ V (the current at $V_g = 0$ V and $V_b = 0.1$ V is used as the reference).

CRediT authorship contribution statement

Hao Wang: Conceptualization, Methodology, Software, Validation, Formal analysis, Investigation, Writing - original draft, Writing - review & editing, Visualization. **Yihan Wang:** Formal analysis, Investigation, Writing - review & editing. **Bin Bai:** Validation, Resources, Supervision, Funding acquisition. **Xun Guo:** Conceptualization, Methodology, Validation, Investigation, Resources, Writing - original draft, Writing - review & editing, Visualization, Supervision, Project administration. **Jianming Xue:** Conceptualization, Validation, Resources, Writing - review & editing, Supervision, Project administration, Funding acquisition.

Declaration of Competing Interest

The authors declare that they have no known competing financial interests or personal relationships that could have appeared to influence the work reported in this paper.

Acknowledgment

This work is financially supported by the Science Challenge Project (Grant No. TZ2018004), National Natural Science Foundation of China (Grant No. 91426304, 11705010), and China Postdoctoral Science Foundation (Grant No. 2019M650351). We are grateful for computing resource provided by Weiming No. 1 and Life Science No. 1 High Performance Computing Platform at Peking University, the National Supercomputer Center in Guangzhou, and TianHe-1(A) at National Supercomputer Center in Tianjin.

Appendix A. Supplementary material

Supplementary data associated with this article can be found, in the online version, at https://doi.org/10.1016/j.apsusc.2020.147347.

References

[1] K.S. Novoselov, A.K. Geim, S.V. Morozov, D. Jiang, Y. Zhang, S.V. Dubonos, I.V. Grigorieva, A.A. Firsov, Electric field effect in atomically thin carbon films, Science 306 (5696) (2004) 666–669.
[2] A.K. Geim, K.S. Novoselov, The rise of graphene, Nat. Mater. 6 (2007) 183, https://doi.org/10.1038/nmat1849.
[3] F. Xia, D.B. Farmer, Y.M. Lin, P. Avouris, Graphene field-effect transistors with high on/off current ratio and large transport band gap at room temperature, Nano Lett. 10 (2) (2010) 715–718, https://doi.org/10.1021/nl9039636.
[4] Z. Li, F. Chen, Ion beam modification of two-dimensional materials: characterization, properties, and applications, Appl. Phys. Rev. 4 (1) (2017) 011103.
[5] I. Childres, L.A. Jauregui, M. Foxe, J. Tian, R. Jalilian, I. Jovanovic, Y.P. Chen, Effect of electron-beam irradiation on graphene field effect devices, Appl. Phys. Lett. 97 (17) (2010) 173109.
[6] Y. Naitou, T. Iijima, S. Ogawa, Direct nano-patterning of graphene with helium ion beams, Appl. Phys. Lett. 106 (3) (2015) 033103.

[7] G. Nanda, S. Goswami, K. Watanabe, T. Taniguchi, P.F. Alkemade, Defect control and n-doping of encapsulated graphene by helium-ion-beam irradiation, Nano Lett. 15 (6) (2015) 4006–4012, https://doi.org/10.1021/acs.nanolett.5b00939.

[8] P. Willke, J.A. Amani, A. Sinterhauf, S. Thakur, T. Kotzott, T. Druga, S. Weikert, K. Maiti, H. Hofsass, M. Wenderoth, Doping of graphene by low-energy ion beam implantation: structural, electronic, and transport properties, Nano Lett. 15 (8) (2015) 5110–5115, https://doi.org/10.1021/acs.nanolett.5b01280.

[9] A. Butenko, E. Zion, Y. Kaganovskii, L. Wolfson, V. Richter, A. Sharoni, E. Kogan, M. Kaveh, I. Shlimak, Influence of ageing on raman spectra and the conductivity of monolayer graphene samples irradiated by heavy and light ions, J. Appl. Phys. 120 (4) (2016) 044306.

[10] P. Ernst, R. Kozubek, L. Madauß, J. Sonntag, A. Lorke, M. Schleberger, Irradiation of graphene field effect transistors with highly charged ions, Nucl. Instrum. Methods Phys. Res., Sect. B 382 (2016) 71–75.

[11] S. Kumar, A. Kumar, A. Tripathi, C. Tyagi, D. Avasthi, Engineering of electronic properties of single layer graphene by swift heavy ion irradiation, J. Appl. Phys. 123 (16) (2018) 161533.

[12] J. Zhao, H. Zeng, B. Li, J. Wei, J. Liang, Effects of stone-wales defect symmetry on the electronic structure and transport properties of narrow armchair graphene nanoribbon, J. Phys. Chem. Solids 77 (2015) 8–13, https://doi.org/10.1016/j.jpcs.2014.08.010.

[13] J.-H. Chen, C. Jang, S. Adam, M. Fuhrer, E. Williams, M. Ishigami, Charged-impurity scattering in graphene, Nat. Phys. 4 (5) (2008) 377.

[14] A. Cresti, N. Nemec, B. Biel, G. Niebler, F. Triozon, G. Cuniberti, S. Roche, Charge transport in disordered graphene-based low dimensional materials, Nano Res. 1 (5) (2008) 361–394.

[15] V.M. Pereira, J.L. Dos Santos, A.C. Neto, Modeling disorder in graphene, Phys. Rev. B 77 (11) (2008) 115109.

[16] J.H. Chen, W.G. Cullen, C. Jang, M.S. Fuhrer, E.D. Williams, Defect scattering in graphene, Phys. Rev. Lett. 102 (23) (2009) 236805, https://doi.org/10.1103/PhysRevLett.102.236805.

[17] Y.B. Zhou, Z.M. Liao, Y.F. Wang, G.S. Duesberg, J. Xu, Q. Fu, X.S. Wu, D.P. Yu, Ion irradiation induced structural and electrical transition in graphene, J. Chem. Phys. 133 (23) (2010) 234703, https://doi.org/10.1063/1.3518979.

[18] G. Buchowicz, P.R. Stone, J.T. Robinson, C.D. Cress, J.W. Beeman, O.D. Dubon, Correlation between structure and electrical transport in ion-irradiated graphene grown on cu foils, Appl. Phys. Lett. 98 (3) (2011) 032102.

[19] A. Lherbier, S.M. Dubois, X. Declerck, S. Roche, Y.M. Niquet, J.C. Charlier, Two-dimensional graphene with structural defects: elastic mean free path, minimum conductivity, and anderson transition, Phys. Rev. Lett. 106 (4) (2011) 046803, https://doi.org/10.1103/PhysRevLett.106.046803.

[20] A. Lherbier, S.M.-M. Dubois, X. Declerck, Y.-M. Niquet, S. Roche, J.-C. Charlier, Transport properties of graphene containing structural defects, Phys. Rev. B 86 (7) (2012) 075402.

[21] S. Nakaharai, T. Iijima, S. Ogawa, S. Suzuki, S.-L. Li, K. Tsukagoshi, S. Sato, N. Yokoyama, Conduction tuning of graphene based on defect-induced localization, ASC Nano 7 (7) (2013) 5694–5700.

[22] Y. Naitou, S. Ogawa, Anderson localization of graphene by helium ion irradiation, Appl. Phys. Lett. 108 (17) (2016) 171605.

[23] E. Zion, A. Haran, A.V. Butenko, L. Wolfson, Y. Kaganovskii, T. Havdala, A. Sharoni, D. Naveh, V. Richter, M. Kaveh, Localization of charge carriers in monolayer graphene gradually disordered by ion irradiation, Graphene 4 (2015) 45–53, https://doi.org/10.4236/graphene.2015.43005.

[24] S.B. Desai, S.R. Madhvapathy, A.B. Sachid, J.P. Llinas, Q. Wang, G.H. Ahn, G. Pitner, M.J. Kim, J. Bokor, C. Hu, Mos2 transistors with 1-nanometer gate lengths, Science 354 (6308) (2016) 99–102.

[25] R.K. Cavin, P. Lugli, V.V. Zhirnov, Science and engineering beyond moore's law, Proceedings of the IEEE 100 (Special Centennial Issue) (2012) 1720–1749, https://doi.org/10.1109/JPROC.2012.2190155.

[26] M.M. Waldrop, The chips are down for moore's law, Nature News 530 (7589) (2016) 144.

[27] D. Saha, S. Mahapatra, Theoretical insights on the electro-thermal transport properties of monolayer mos2 with line defects, J. Appl. Phys. 119 (13) (2016) 134304, https://doi.org/10.1063/1.4945582.

[28] J. Jiang, R. Pachter, T. Demeritte, P.C. Ray, A.E. Islam, B. Maruyama, J.J. Boeckl, Modeling graphene with nanoholes: structure and characterization by raman spectroscopy with consideration for electron transport, J. Phys. Chem. C 120 (10) (2016) 5371–5383.

[29] J.P. Mendez, F. Arca, J. Ramos, M. Ortiz, M.P. Ariza, Charge carrier transport across grain boundaries in graphene, Acta Mater. 154 (2018) 199–206, https://doi.org/10.1016/j.actamat.2018.05.019.

[30] E. Zaminpayma, M.E. Razavi, P. Nayebi, Electronic properties of graphene with single vacancy and stone-wales defects, Appl. Surf. Sci. 414 (2017) 101–106.

[31] A. Hashimoto, K. Suenaga, A. Gloter, K. Urita, S. Iijima, Direct evidence for atomic defects in graphene layers, Nature 430 (7002) (2004) 870.

[32] L. Li, S. Reich, J. Robertson, Defect energies of graphite: density-functional calculations, Phys. Rev. B 72 (18) (2005) 184109.

[33] J.C. Meyer, C. Kisielowski, R. Erni, M.D. Rossell, M. Crommie, A. Zettl, Direct imaging of lattice atoms and topological defects in graphene membranes, Nano Lett. 8 (11) (2008) 3582–3586.

[34] F. Banhart, J. Kotakoski, A.V. Krasheninnikov, Structural defects in graphene, ASC Nano 5 (1) (2010) 26–41.

[35] T.O. Wehling, S. Yuan, A.I. Lichtenstein, A.K. Geim, M.I. Katsnelson, Resonant scattering by realistic impurities in graphene, Phys. Rev. Lett. 105 (5) (2010) 056802, https://doi.org/10.1103/PhysRevLett.105.056802.

[36] M. Brandbyge, J.-L. Mozos, P. Ordejón, J. Taylor, K. Stokbro, Density-functional method for nonequilibrium electron transport, Phys. Rev. B 65 (16) (2002) 165401.

[37] D. Stradi, U. Martinez, A. Blom, M. Brandbyge, K. Stokbro, General atomistic approach for modeling metal-semiconductor interfaces using density functional theory and nonequilibrium green's function, Phys. Rev. B 93 (15) (2016) 155302.

[38] S. Haldar, R.G. Amorim, B. Sanyal, R.H. Scheicher, A.R. Rocha, Energetic stability, stm fingerprints and electronic transport properties of defects in graphene and silicene, RSC Adv. 6 (8) (2016) 6702–6708, https://doi.org/10.1039/C5RA23052G.

[39] QuantumATK version Q-2018.6, Synopsys QuantumATK (www.synopsys.com/silicon/quantumatk.html).

[40] S. Smidstrup, T. Markussen, P. Vancraeyveld, J. Wellendorff, J. Schneider, T. Gunst, B. Verstichel, D. Stradi, P.A. Khomyakov, U.G. Vej-Hansen, et al., Quantumatk: An integrated platform of electronic and atomic-scale modelling tools, J. Phys.: Condens. Matter 32 (2020) 015901.

[41] S. Smidstrup, D. Stradi, J. Wellendorff, P.A. Khomyakov, U.G. Vej-Hansen, M.-E. Lee, T. Ghosh, E. Jónsson, H. Jónsson, K. Stokbro, First-principles green's-function method for surface calculations: a pseudopotential localized basis set approach, Phys. Rev. B 96 (19) (2017) 195309, https://doi.org/10.1103/PhysRevB.96.195309.

[42] J.P. Perdew, K. Burke, M. Ernzerhof, Generalized gradient approximation made simple, Phys. Rev. Lett. 77 (18) (1996) 3865–3868, https://doi.org/10.1103/PhysRevLett.77.3865.

[43] M. Fuchs, M. Scheffler, Ab initio pseudopotentials for electronic structure calculations of poly-atomic systems using density-functional theory, Comput. Phys. Commun. 119 (1) (1999) 67–98, https://doi.org/10.1016/S0010-4655(98)00201-X.

[44] J. Li, L.-C. Xu, Y. Yang, X. Liu, Z. Yang, The transport and optoelectronic properties of γ-graphyne-based molecular magnetic tunnel junctions, Carbon 132 (2018) 632–640, https://doi.org/10.1016/j.carbon.2018.02.094.

[45] Z.-Q. Fan, W.-Y. Sun, X.-W. Jiang, Z.-H. Zhang, X.-Q. Deng, G.-P. Tang, H.-Q. Xie, M.-Q. Long, Redox control of magnetic transport properties of a single anthraquinone molecule with different contacted geometries, Carbon 113 (2017) 18–25, https://doi.org/10.1016/j.carbon.2016.11.021.

[46] Z.-Q. Fan, W.-Y. Sun, Z.-H. Zhang, X.-Q. Deng, G.-P. Tang, H.-Q. Xie, Symmetry-dependent spin transport properties of a single phenalenyl or pyrene molecular device, Carbon 122 (2017) 687–693, https://doi.org/10.1016/j.carbon.2017.07.019.

[47] J. Li, Z.H. Zhang, X.Q. Deng, Z.Q. Fan, G.P. Tang, Magnetic transport properties of a trigonal graphene sandwiched between graphene nanoribbon electrodes, Carbon 93 (2015) 335–341, https://doi.org/10.1016/j.carbon.2015.05.050.

[48] S. Wen, F. Gao, C. Yam, S. Gao, Nanomechanical control of spin current flip using monovacancy graphene, Carbon 133 (2018) 218–223, https://doi.org/10.1016/j.carbon.2018.03.007.

[49] R. Hu, Z.Q. Fan, C.H. Fu, L.Y. Nie, W.R. Huang, Z.H. Zhang, Structural stability, magneto-electronics and spin transport properties of triangular graphene nanoflake chains with edge oxidation, Carbon 126 (2018) 93–104, https://doi.org/10.1016/j.carbon.2017.10.018.

[50] M.J. van Setten, M. Giantomassi, E. Bousquet, M.J. Verstraete, D.R. Hamann, X. Gonze, G.M. Rignanese, The pseudodojo: Training and grading a 85 element optimized norm-conserving pseudopotential table, Comput. Phys. Commun. 226 (2018) 39–54, https://doi.org/10.1016/j.cpc.2018.01.012.

[51] D.R. Hamann, Optimized norm-conserving vanderbilt pseudopotentials, Phys. Rev. B 88 (8) (2013) 085117, https://doi.org/10.1103/PhysRevB.88.085117.

[52] M. Schlipf, F. Gygi, Optimization algorithm for the generation of oncv pseudopotentials, Comput. Phys. Commun. 196 (2015) 36–44, https://doi.org/10.1016/j.cpc.2015.05.011.

[53] D.C. Liu, J. Nocedal, On the limited memory bfgs method for large scale optimization, Math. Program. 45 (1) (1989) 503–528, https://doi.org/10.1007/BF01589116.

[54] H.J. Monkhorst, J.D. Pack, Special points for brillouin-zone integrations, Phys. Rev. B 13 (12) (1976) 5188–5192, https://doi.org/10.1103/PhysRevB.13.5188.

[55] S. Datta, Electronic Transport in Mesoscopic Systems, Cambridge University Press, 1997.

[56] D. Çakır, F.M. Peeters, Dependence of the electronic and transport properties of metal-mose$_2$ interfaces on contact structures, Phys. Rev. B 89 (24) (2014) 245403, https://doi.org/10.1103/PhysRevB.89.245403.

[57] A.R. Botello-Méndez, A. Lherbier, J.-C. Charlier, Modeling electronic properties and quantum transport in doped and defective graphene, Solid State Commun. 175 (2013) 90–100.

[58] Z. Li, H. Qian, J. Wu, B.-L. Gu, W. Duan, Role of symmetry in the transport properties of graphene nanoribbons under bias, Phys. Rev. Lett. 100 (20) (2008) 206802.

[59] N.D. Mermin, H. Wagner, Absence of ferromagnetism or antiferromagnetism in one- or two-dimensional isotropic heisenberg models, Phys. Rev. Lett. 17 (22) (1966) 1133.

[60] R. Faccio, A.W. Mombru, Magnetism in multivacancy graphene systems, J. Phys.: Condens. Matter 24 (37) (2012) 375304, https://doi.org/10.1088/0953-8984/24/37/375304.

[61] S. Ghosh, I. Calizo, D. Teweldebrhan, E.P. Pokatilov, D.L. Nika, A.A. Balandin, W. Bao, F. Miao, C.N. Lau, Extremely high thermal conductivity of graphene: Prospects for thermal management applications in nanoelectronic circuits, Appl. Phys. Lett. 92 (15) (2008) 151911, https://doi.org/10.1063/1.2907977.

[62] C. Si, Z. Liu, W. Duan, F. Liu, First-principles calculations on the effect of doping and biaxial tensile strain on electron-phonon coupling in graphene, Phys. Rev. Lett. 111 (19) (2013) 196802, https://doi.org/10.1103/PhysRevLett.111.196802.

[63] F.V. Tikhonenko, A.A. Kozikov, A.K. Savchenko, R.V. Gorbachev, Transition between electron localization and antilocalization in graphene, Phys. Rev. Lett. 103

(22) (2009) 226801, https://doi.org/10.1103/PhysRevLett.103.226801.
[64] E.H. Hwang, S. Das Sarma, Acoustic phonon scattering limited carrier mobility in two-dimensional extrinsic graphene, Phys. Rev. B 77 (11) (2008) 115449, https://doi.org/10.1103/PhysRevB.77.115449.
[65] J.-H. Chen, C. Jang, S. Xiao, M. Ishigami, M.S. Fuhrer, Intrinsic and extrinsic performance limits of graphene devices on sio2, Nat. Nanotechnol. 3 (2008) 206, https://doi.org/10.1038/nnano.2008.58.
[66] S.V. Morozov, K.S. Novoselov, M.I. Katsnelson, F. Schedin, D.C. Elias, J.A. Jaszczak, A.K. Geim, Giant intrinsic carrier mobilities in graphene and its bilayer, Phys. Rev. Lett. 100 (1) (2008) 016602, https://doi.org/10.1103/PhysRevLett.100.016602.
[67] S.N. Shirodkar, U.V. Waghmare, Electronic and vibrational signatures of stone-wales defects in graphene: First-principles analysis, Phys. Rev. B 86 (16) (2012) 165401.
[68] L. Liu, M. Qing, Y. Wang, S. Chen, Defects in graphene: generation, healing, and their effects on the properties of graphene: a review, J. Mater. Sci. Technol. 31 (6) (2015) 599–606.
[69] Z. Bai, L. Zhang, L. Liu, Bombarding graphene with oxygen ions: combining effects of incident angle and ion energy to control defect generation, J. Phys. Chem. C 119 (47) (2015) 26793–26802, https://doi.org/10.1021/acs.jpcc.5b09620.
[70] B. Wang, Y. Puzyrev, S.T. Pantelides, Strain enhanced defect reactivity at grain boundaries in polycrystalline graphene, Carbon 49 (12) (2011) 3983–3988, https://doi.org/10.1016/j.carbon.2011.05.038.
[71] M.T. Lusk, L.D. Carr, Nanoengineering defect structures on graphene, Phys. Rev. Lett. 100 (17) (2008) 175503, https://doi.org/10.1103/PhysRevLett.100.175503.
[72] F. Banhart, J. Kotakoski, A.V. Krasheninnikov, Structural defects in graphene, ACS Nano 5 (1) (2011) 26–41, https://doi.org/10.1021/nn102598m.
[73] B.W. Jeong, J. Ihm, G.-D. Lee, Stability of dislocation defect with two pentagon-heptagon pairs in graphene, Phys. Rev. B 78 (16) (2008) 165403, https://doi.org/10.1103/PhysRevB.78.165403.
[74] S.J. Rodríguez, E.A. Albanesi, Electronic transport in a graphene single layer: application in amino acid sensing, Phys. Chem. Chem. Phys. 21 (2) (2019) 597–606, https://doi.org/10.1039/C8CP05093G.